RESEARCH PAPER

CrossMark

Effect of processing temperatures on the properties of a high-strength steel welded by FSW

Gonçalo Sorger [1] · Teemu Sarikka [1] · Pedro Vilaça [1] (iD) · Telmo G. Santos [2]

Abstract

The need for weight reduction without compromising load-bearing capacity has driven the development of modern high-strength steels (HSS). The ability to take full advantage of these modern HSS is limited by their weldability. Friction stir welding (FSW) can join HSS at low peak temperatures, better preserving the properties of the base material. This work evaluates the influence of different FSW peak temperatures and cooling rates on the properties of a modern HSS. A HSS produced by a thermo-mechanically controlled process was welded by FSW with peak temperatures, measured within the processed zone, ranging from about 900 to 650 °C. Temperatures were measured using thermocouples positioned at the mid-thickness of the workpiece, at 5 to 10 mm from the joint line. The effect of the different peak temperatures was evaluated by mechanical testing, including bending, tensile testing with digital imaging correlation, Charpy impact test, and hardness measurements. Microscopic analyses, including optical microscopy and electron backscatter diffraction, were used to evaluate the microstructure. Results show that FSW enables welding HSS within the intercritical temperature domain. The impact toughness of the best weld condition overmatched the base material by over 37%, at both − 40 and − 60 °C. The yield strength efficiency was about 70%.

Keywords Friction stir welding · High-strength steels · Mechanical properties · Microstructure · Temperature

1 Introduction

Welding is the main manufacturing technique applied in the production of large and complex steel structures. New ultra-high-strength steels (UHSS) offer superior mechanical properties enabling leaner, lighter, and, therefore, more cost-efficient structures for a wide range civil, marine, offshore, and other applications. These steels, manufactured using accelerated cooling to achieve the desired microstructures, are generally not resistant to high heat inputs and, as a result, welding by conventional fusion processes can degrade their properties. The weldability of these UHSS is, therefore, a critical characteristic that is currently limiting their widespread use [1]. This limitation can be overcome by friction stir welding, an autogenous solid-state process that can join these materials at low temperatures and with some control of the cooling rates. Compared to conventional fusion welding methods, FSW has a high thermal efficiency (over 90% when applied to aluminum alloys [2]) and produces welds with significantly lower peak temperature and lower heat input dissipated into the heat-affected zone (HAZ).

The distinction between high-strength steel (HSS) and UHSS has not been universally defined by one precise strength level. A universal yield strength limit would be difficult to define since the strength levels of special steels are continuously increasing as new steels are developed [3]. The steel studied in this paper has a yield strength of 700 MPa and was produced via thermo-mechanically controlled processing (TMCP). This steel is considered an UHSS based on the classification in reference [4], where the minimum yield strength for UHSS is 550 MPa. However, in some classifications, considerably higher yield strengths are required. For example, in [5], yield strength of 900 MPa is necessary for a steel to be classified as an UHSS.

✉ Gonçalo Sorger
goncalo.sorger@aalto.fi

[1]   Department of Mechanical Engineering, School of Engineering, Aalto University, 02150 Espoo, Finland

[2]   UNIDEMI, Departamento de Engenharia Mecânica e Industrial, Faculdade de Ciências e Tecnologia, Universidade Nova de Lisboa, 2829-516 Caparica, Portugal

⚘ Springer

TMCP is currently a common production method for HSS and UHSS since it enables the production of fine-grained steels. Through this method, high-strength steels can be achieved even with low levels of alloying. Additionally, this is not accomplished at the expense of toughness since grain size is the key factor in attaining the high-strength properties [1, 6]. The lower amounts of alloying elements have the further advantage of reducing production costs [7, 8]. However, these steels are quite sensitive to the peak temperatures and cooling rates. Welding by conventional fusion processes can degrade their properties destroying the original optimized grain size and good balance of strength and toughness [1]. Friction stir welding (FSW), due to its solid-state process domain and autogenous nature, can join these materials at significantly lower temperatures and with some control of the cooling rates, e.g., via active cooling, overcoming the weldability limitations of conventional fusion welding methods.

FSW is nowadays widely used across many market sectors in the fabrication of safety critical structures, mostly applied to lightweight metals and their alloys [9]. FSW of aluminum [10, 11], copper [12, 13], and magnesium [14] has had excellent results once the operational parameters have been optimized. This success increased the interest in transferring the benefits of the process to other engineering materials, such as modern steels. The lower processing temperatures associated with FSW (compared to fusion welding processes) have the potential to produce fewer metallurgical changes in the weld metal and HAZ and minimize distortion and residual stresses in steels [15]. Furthermore, the absence of melting eliminates the susceptibility to hot cracking and hydrogen induced cracking in steels. Additionally, it also produces less hazardous fume emissions [16].

It was only in 1999 that the feasibility of FSW of steel was first reported in open literature. Thomas et al. [17] showed that 12 mm plain low carbon steel and 12% chromium alloy steel can be welded in a single pass, and demonstrated, by tensile and bend testing, that the mechanical properties of the welded joints can be compared to those of the base material. Tool wear was identified as a limitation but recent advances in material selection and design have led to the development of tools with a fine balance of high-temperature strength, hardness, and ductility enabling the production of long uninterrupted FSW steel welds [18, 19].

Compared to fusion welding, FSW typically produces less distortion, is not detrimental to toughness, and does not cause concerning levels of hardness. Additionally, FSW can generate superior fatigue properties [20]. The solid-state nature of the process can enable joining the TMCP steels in the same range of temperatures where they are originally processed, i.e., the intercritical temperature region (ferrite austenite two-phase region) between the A_1 and A_3 temperatures [6]. FSW of UHSS in their optimal range of thermomechanical processing conditions could result in welds with fine microstructure enabling a good combination of high-strength and toughness.

Furthermore, FSW is an autogenous process (i.e., it requires no filler metal), which helps to reduce or eliminate the chemical and mechanical mismatch in the processed zone.

Studies on FSW of steels, such as the ones by Lienert et al. [21] and Reynolds et al. [22], report that the stirred zone of ferrous metals displays a recrystallized microstructure. This indicates that FSW of ferrous metals develops in a similar way to that of aluminum alloys. The trend is analogous to that observed with aluminum alloys, where the grain size decreases and the strength gradually increases [23, 24]. Additionally, during the FSW of steel, the thermomechanical processing can induce complex phase transformations leading to the improvement of mechanical properties.

The microstructure and mechanical properties of FSW joints on carbon steel are known to be affected by the welding conditions [25–27]. The strength of the steel joints increases with the decreasing peak temperatures [25]. This is attributed to the relationship between the peak temperature and the intercritical temperature domain. When FSW is performed within this temperature domain, between A_1 and A_3, the microstructure is refined and the highest strength is achieved [26]. Although in [26] FSW was applied to mild steels (IF steel, S12C and S35C), it is reasonable to assume that FSW of TMCP HSS with low heat input (resulting in peak temperatures between A_1 and A_3) would have a similar, if not more relevant, effect. Since the improved properties of HSS typically result from thermomechanical processing within the A_1 to A_3 temperature range, FSW in this range of temperatures should prevent a significant loss of the original microstructure, including the small grain size. Additional evidence of the benefits, for UHSS, of FSW at temperatures within the intercritical temperature domain was presented in [28]. FSW joints were performed on a 2.2-mm sheet metal quenched and tempered UHSS, with specified minimum yield strength of 1600 MPa. The authors reported that the weldability of that steel is not feasible below the A_1 temperature. The microstructure of the stirred zone processed above A_1 was akin to that of the base material, with fine martensite and a low amount of retained austenite. Accordingly, both the impact load and absorbed energy for the stir zone are about the same as the base metal. Thus, the main motivation for this research work is to evaluate the same potential benefits when applying the FSW to a thicker, 4 mm, HSS plate with a specified minimum yield stress of 700 MPa.

In this work, the influence of different peak temperatures and heating and cooling rates achieved during the FSW cycles was evaluated. A TMCP HSS with a specified minimum yield stress of 700 MPa was welded by FSW under different conditions resulting in peak temperatures, in the close vicinity of the processed zone, ranging from about 650 to 900 °C. The effect of the different peak temperatures and heating and cooling rates on the microstructure and properties was investigated.

2 Experimental procedure

HSS plates were joined by FSW under four different conditions, combining a set of two parameters (rotation speed, Ω, and travel speed, v) with and without active cooling provided by water-cooled anvil and clamping system. The temperature was monitored in different key positions of the processed zone and specimens were extracted for mechanical and microstructural characterization. The tests include bending, tensile, Charpy impact, hardness, optical microscopy (OM), and electron backscatter diffraction (EBSD).

2.1 Material

The material studied in this paper was the Strenx 700MC+, from SSAB, a modern hot-rolled structural HSS produced by TMCP. This direct quenched steel, with nominal chemical composition presented in Table 1, fulfills the requirements of the S700MC grade according to standard EN 10149-2. The plate thickness was 4 mm. Research on the weldability of this steel, in different thicknesses, by MIG, PAW, and SAW was carried out by Peltonen [29] and Lathtinen [30].

2.2 FSW procedure specification

The weld runs were performed in force control, using an ESAB Legio 5 UT FSW machine. The plate dimensions before welding were $330 \times 100 \times 4$ mm. Specimens welded with four different conditions were tested. The different welding conditions were designated as (1) "Slow"; (2) "Fast"; (3) "Slow + Cooled"; and (4) "Fast + Cooled" according to their different welding parameters (travel speeds) and external forced cooling condition, as summarized in Table 2. Rotation speed was kept constant at $\Omega = 200$ rpm. The weld pitch ratio (Ω/v) used for the slow (hotter) welds was (Ω/v)$_{slow} = 3.33$, and for the fast (colder) welds was (Ω/v)$_{fast} = 1.67$. All welds were made along the rolling direction of the plates, in single-pass square butt joints, in flat position. Edge preparation was done by machining. The plates were firmly clamped with mechanical fixtures and dedicated water cooled clamping elements and backing bar that enable active cooling, as depicted in Fig. 1a. The plates were joined using a tool made from pcBN-based W-Re composite materials with 70 vol.% pcBN [20]. The tool has a scrolled convex shoulder (enabling tilt angle = 0°) with outer diameter of 25 mm and a 3.75-mm-long conical probe with stepped spiral features (Fig. 1b). Argon was used as shielding gas for the tool and the top surface of the processed zone, flowing at 20 L/min out of a nozzle with diameter of 70 mm that envelops the body of the FSW tool. The parameters used during the plunging period were as follows: rotation speed $\Omega = 800$ rpm, plunging speed $v_z = 0.1$ mm/s, plunging depth $z_{plunge} = 3.9$ mm and dwell time $t_{dwell} = 3$ s. The weld length was 290 mm starting and ending 20 mm from the edge of the plates. Three identical welds were done for each of the four welding conditions. Of those three, the first was used for temperature measurements and to extract samples for bending tests. The remaining two welded plates were used for extraction of samples for tensile, Charpy impact, and microscopy testing.

2.3 Temperature measurements

Temperatures were measured at the half-thickness of the plates and at four different distances from the original abutting surfaces using insulated N-type thermocouples. The temperature measurement positions were ± 10, ± 8, ± 6, and ± 5 mm, where the positive (+) values represent temperatures measured at the advancing side (AS) and the negative (−) values represent temperatures measured at the retreating side (RS). These positions were chosen considering the tool geometry, to attempt to encompass all the different welding zones, while minimizing any disturbance to the material flow during the FSW process, i.e., avoiding direct contact with the probe (Fig. 2a). Each measurement position was repeated once, for redundancy. Accurate positioning of the thermocouples was possible by employing a backing plate with grooves machined for the thermocouple wires and by drilling holes in the weld plates at the desired temperature measurement positions and depth as depicted in Fig. 2b. The spacing between measurement positions along the weld direction was 25 mm, over one shoulder diameter, to ensure no coercive effects in the thermal field between the different thermocouples.

2.4 Mechanical testing and microscopy

Bending testing Specimens for bending tests were extracted from the temperature measurement welds at positions that were unaffected by the thermocouple positioning holes. For each of the four welding conditions, six bending specimens were tested, three with the tension stress at the face side and

Table 1 Chemical composition of the S700MC (wt%), according to melting analysis conducted by SSAB in Raahe, Finland. CE$_{IIW}$ [31] is the carbon equivalent as adopted by International Institute of Welding

Material S700MC	C	Si	Mn	Cr	Nb	Ti	V	Al
	0.056	0.179	1.8	0.048	0.082	0.112	0.012	0.036
	Cu	Ni	Mo	N	B	P	S	CE$_{IIW}$
	0.016	0.035	0.009	0.0068	0.0003	0.009	0.0022	0.241

Table 2 Sets of FSW parameters for the different weld conditions

FSW condition	F [kN]	Tilt angle [°]	Ω [rpm]	v [mm/min]	Cooling
Slow	45	0	200	60	Off
Fast				120	Off
Slow + Cooled				60	On
Fast + Cooled				120	On

three with tension at the root side. The bending tests were carried out according to standard ISO 5173 + A1, using a MTS 810 Material Test System at a constant speed of 0.2 mm/s. The maximum displacement of the loading pin was restricted to 60 mm from the starting position contacting the surface of the specimens.

Tensile testing and DIC measurements Specimens for tensile testing were extracted according to the extraction plan presented in Fig. 3a. The tensile tests were conducted using a MTS Landmark machine. A 25-mm extensometer was used to register the strain rate. Digital image correlation (DIC) measurements were performed during the tensile test on one specimen of each condition. To this end, a random pattern was spray painted on the specimens over a white paint substrate. A Lavision Imager Pro X camera system recorded images of the specimens at the frequency of 2 Hz. Based on changes in the pattern with increasing strain, the behavior of the strain and its localization was estimated by analyzing the images using DaVis software.

Charpy impact testing Charpy impact tests were conducted according to standard ISO 148-1. Due to constraints posed by plate thickness, a reduced-section specimen was used: $55 \times 10 \times 4$ [mm]. The notches were placed at three different positions as illustrated in Fig. 3b, corresponding to the center of the stirred zone (SZ), center − 5 mm at the RS, and center +5 mm at the AS. The specimens were tested at − 40 and − 60 °C. Due to the non-standard size of the specimens, and to allow for a

meaningful comparison and interpretation of the results, specimens with the same geometry extracted from base material were also tested.

Hardness Microhardness measurements were performed using an instrumented tester and a Vickers tip. The step size between each indentation was 0.5 mm and the indentation load was 5 N, producing indentations with a cross-section diagonal of approximately 50 μm in the base metal. The measurement matrices, containing 315 indentations, covered a 22.5 mm by 3.5 mm area encompassing the different weld zones and the BM on both sides of the weld. The hardness values measured with the instrumented tester are presented in units of HVIT, which for an indentation load of 5 N is roughly equivalent to HV05.

OM and EBSD Specimens for optical microscopy were polished down to 1 μm diamond paste and etched with 2% Nital solution. Optical micrographs were taken using an Olympus CX40 microscope. The microscope was equipped with Olympus MPlan metallurgical lenses. SEM/EBSD was carried out using a Zeiss Ultra 55 field emission scanning electron microscope (FESEM) equipped with an HKL Nordlys EBSD detector by Oxford Instruments. Sample preparation for EBSD was conducted using a mechanical vibratory fine polishing to ensure a deformation-free surface to obtain a sufficiently high diffraction pattern quality. The EBSD data was post-processed using Channel 5 post-processing software.

3 Analysis of results

3.1 Temperature measurements

The highest temperatures in all the weld conditions were measured by the thermocouples positioned closest to the FSW tool, at ± 5 mm distance. The differences between the temperatures measured at the RS and AS are small, less than 25 °C,

Fig. 1 Welding setup and tool for FSW. **a** Details of the clamping system and temperature measurement setup including (1) water cooled clamping elements. The average water temperature was ≈ 7 °C and the flow was 8 L/min; (2) water cooled anvil; (3) shielding gas nozzle; and (4) thermocouple cables. **b** FSW tool with 25 mm shoulder diameter and 10 mm probe root diameter. **c** Perspective of top surface of Fast weld condition
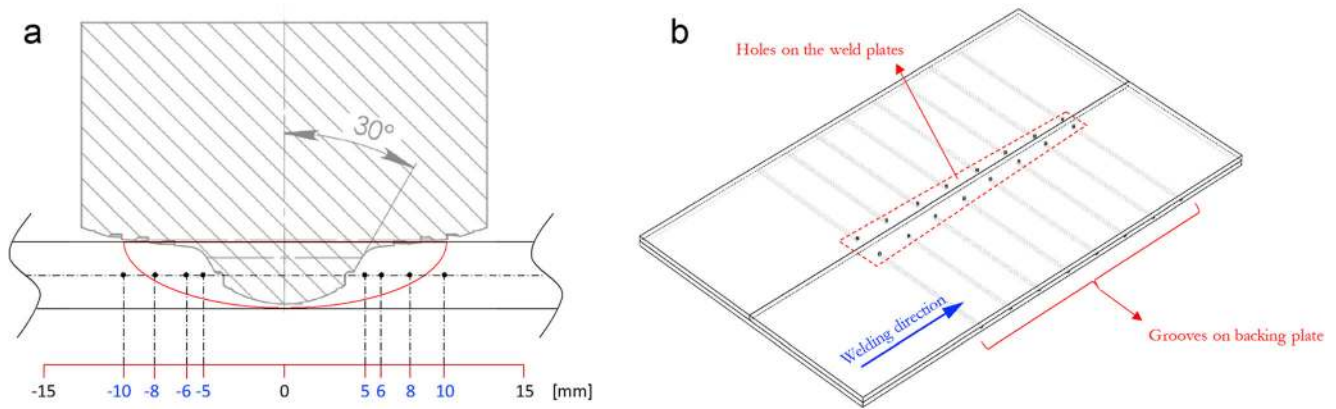
Fig. 2 Schematic representation of the thermocouple positions. **a** Distance of the thermocouples from the joint line. **b** The temperature measurement positions along the weld joint in relation to the weld direction

with slightly higher values at the RS. Thus, for clarity in displaying the data comparing the different weld conditions, only the temperatures acquired at the RS are shown. Table 3 presents the highest temperatures recorded in each weld and the time above the critical temperatures $A_1 = 709$ °C and $A_3 = 871$ °C (calculated according to [32]). The highest peak temperature was reached during the Slow weld, 906.2 °C, while the Fast + Cooled weld achieved the lowest peak temperature, 656.3 °C, below the estimated value for A_1. The Fast and the Slow + Cooled welds reached peak temperatures of 761.1 and 741.1 °C, respectively. This indicates that the active cooling plays a more relevant role than the welding speed in controlling the peak temperature. The active cooling also has a greater influence than the weld pitch ratio (Ω/v) on the thermal cycle, mainly on the duration of the heating period but also on the cooling period. Figure 4a shows that the temperature increase is faster in the + Cooled welds than in the non-cooled welds. Comparing the heating phase of the Fast and the Slow + Cooled welds, which reach similar peak temperatures, further emphasizes this effect. Naturally, the cooling times are also shorter for the + Cooled welds. Given that only the Slow weld reached a peak temperature above 800 °C, it is not

possible to compare the $t_{8/5}$ cooling times for the four welds. Therefore, as an alternative, the cooling times from 600 to 500 °C ($t_{6/5}$) are shown in Fig. 4b.

Comparing the two weld conditions with higher weld pitch ratio (Slow and Slow + Cooled), the cooling rate (averaged between $t_{T=600°C}$ and $t_{T=500°C}$) without active cooling is 18.5 °C/s, and with active cooling it is 41.7 °C/s (an increase of 125%). For the weld conditions with lower weld pitch ratio (Fast and Fast + Cooled), the cooling rate without active cooling is 26.3 °C/s, and with active cooling is 52.6 °C/s (an increase of 100%). According to [32], the value estimated for the M_S temperature is 459 °C. However, as presented in Fig. 4, either the time above the A_1 is too short (less than 15 s for all welds) or the cooling times between A_1 and M_S are too long (over 6 s, for all welds) to reach the M_S temperature without starting other non-martensitic microstructures.

3.2 Microstructure analysis

Macrographs of the four different weld condition cross-sections are shown in Fig. 5. The most significant differences are the width of the stirred zones and HAZ, which are both
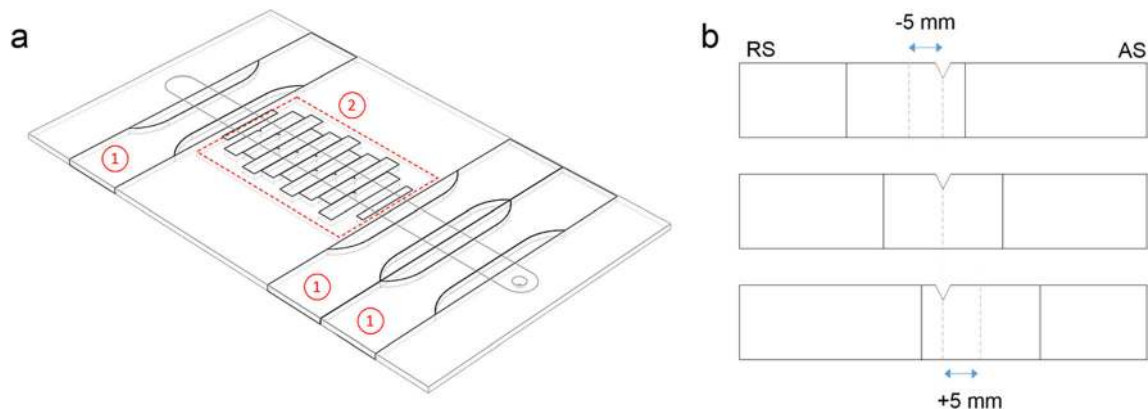

Fig. 3 Schematic representation of test samples. **a** Extraction plan for tensile specimens (1) and Charpy impact specimens (2). **b** Detail of the Charpy notch positions relative to the weld center (stirred zone), weld center +5 mm (advancing side), and weld center − 5 mm (retreating side)

Table 3 Peak temperatures and time above critical temperatures A_1 and A_3 (calculated according to [32]) recorded at the four different weld conditions

Weld	Slow	Fast	Slow + Cooled	Fast + Cooled
T_{max} [°C]	906.2	761.1	741.1	656.3
Time above A_1 [s]	14.3	5.1	2.1	n.a.
Time above A_3 [s]	5.6	n.a	n.a	n.a

n.a not applicable

narrower in the + Cooled welds. This difference in width is very significant at the top surface of the stirred zones. As depicted in Fig. 5, the Slow and Fast weld conditions have about 16 mm in width, and the + Cooled weld conditions have a width of about 12 mm. These results are in agreement with the thermal analysis presented before. With the active cooling, not only are the peak temperatures lower but also the time above critical temperatures is significantly reduced. From the macrographs, it is possible to conclude that the active cooling has a greater effect than changes in travel speed on the overall geometry of the weld beads. Figure 5d, corresponding to the Fast + Cooled weld, reveals the presence of a void defect at the AS of the lower section of the stirred zone. This indicates that the cold weld conditions were taken to an extreme, for the FSW of steels, where the level of viscosity within the stirred material was not low enough for a proper material flow with complete and homogeneous consolidation of the stirred zone.

Another evidence of the effect of temperature is the level of penetration of the stirred zone and processing of the root of the welds. In the Slow and Fast welds, Fig. 6a, b, respectively, there is full penetration with evidence of some small and discontinuous alignment of oxide particles. In contrast, Fig. 6c, d reveals lack of penetration (LOP) defects, mostly in the Slow + Cooled weld. Although the prescribed value for the tool

penetration was the same for all the weld conditions, Figs. 5 and 6 show that, in fact, there are small differences in the level of penetration, which can be related to the precision and stiffness of the welding equipment. This effect is mostly noticeable in the comparison between the Slow + Cooled weld (Fig. 6c) and the Fast + Cooled weld (Fig. 6d).

The microstructure of the HSS base material (BM) consists of fine-grained ferritic-bainitic microstructure produced by rolling and direct quenching. The elongated grains along the rolling direction, presented in Fig. 7a, show evidence of the original TMCP production cycle in the microstructure of the BM. The average grain size of the BM, measured via EBSD, is about 2.6 μm (Fig. 8). Figure 7b–e shows a significant contrast between the microstructure in the stirred zone and the BM. FSW produced a dynamically recrystallized zone, retaining the ferritic-bainitic microstructure, but with an increased presence of ferrite. The grains in the stirred zone are fine equiaxed with sizes of about 2.75 μm for the welds without active cooling and of about 2.3 and 2.1 μm for the slow and fast welds, respectively, with active cooling (Fig. 8). Again, the active cooling played a more relevant role than travel speed in affecting the grain size. Figure 8 shows a relatively homogeneous grain size at the stirred zone for all weld conditions. Nevertheless, across the thermomechanically affected zone (TMAZ) and HAZ, the welds without active cooling exhibit a higher variation of grain size, along a wider distance from the center of the weld bead, as a result of the higher peak temperatures and lower cooling rates, addressed before. Comparing the AS with the RS, the grain size is similar in all zones of the weld, except at the HAZ, where the grain size is slightly larger at the RS, when compared with the AS.

Figure 9 shows EBSD maps for the original HSS and for the stirred zones of the different welding conditions. The band contrast images highlight the grain geometry and size supporting the previous analysis of Fig. 8. The inverse pole figures show a contrast between the orientation of the
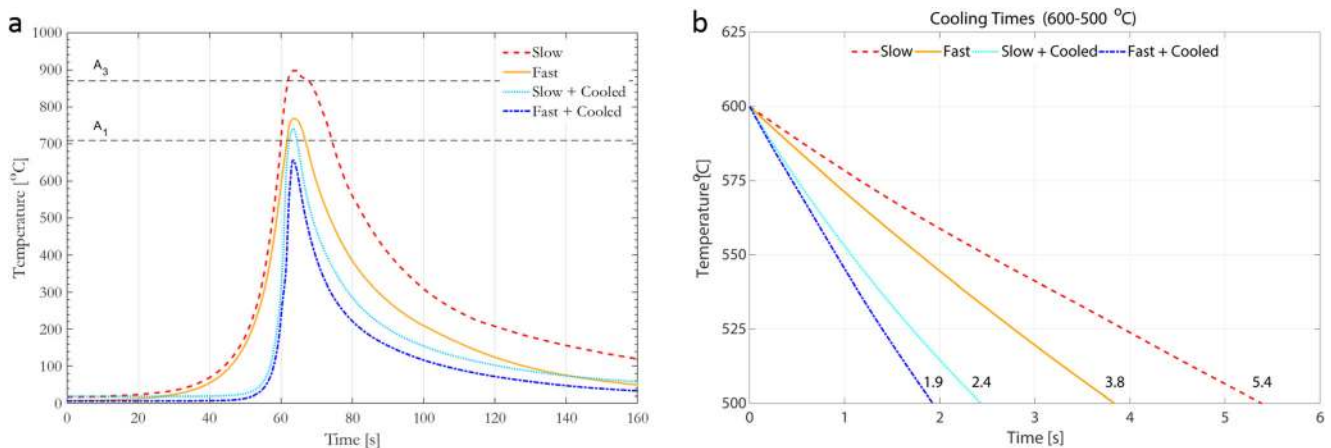

Fig. 4 Results from the temperature monitoring for the different weld conditions at − 5 mm distance from the joint line, at the retreating side (RS). **a** Temperature history. **b** Detail of the cooling times from 600 to 500 °C (t6/5)
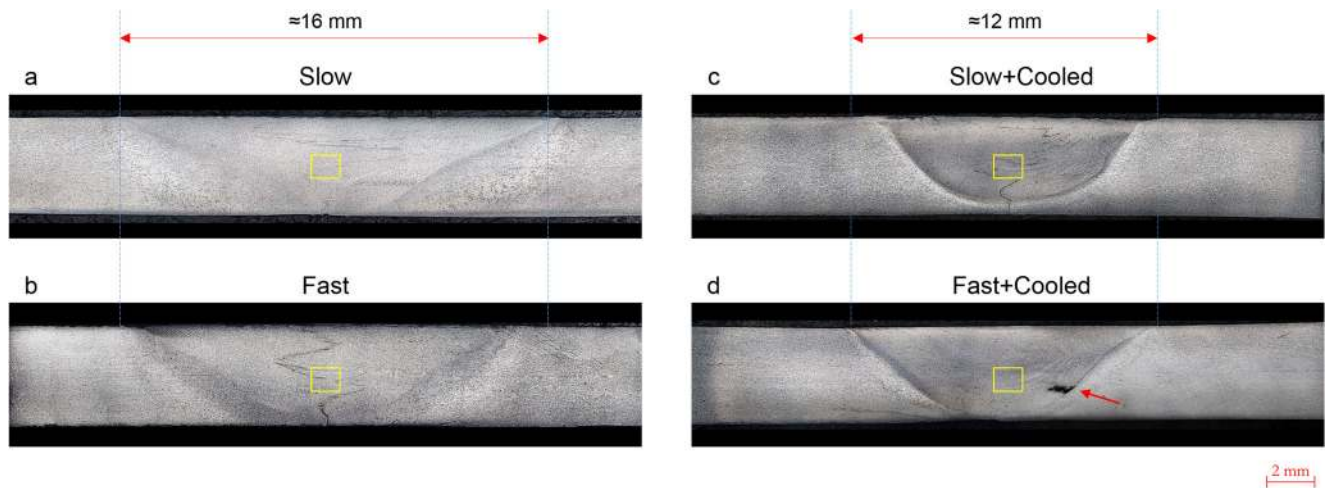
Fig. 5 Macrographs of the cross-section of each of the four different weld conditions (yellow square marks the position of micrographs and EBSD maps). **a** Slow weld with full penetration. **b** Fast weld with full penetration. **c** Slow + Cooled weld with incomplete penetration. **d** Fast + Cooled weld, with quasi-complete penetration, and with an arrow pointing to a void defect

microstructure of the BM, where a texture effect exists with dominating <101> direction, and that of the stirred zones with more randomly oriented grains. The local misorientation maps show a higher local concentration of strain (green color) in the base material than in the stirred zone of the welds.

3.3 Hardness test results

Figure 10 shows the hardness maps of the cross-sections from the four different weld conditions. The base material hardness is about 275 HVIT. The pattern is similar in all the welds, with a lower hardness in the stirred zone, 220 HVIT, increasing sharply from the boundary of the TMAZ into the HAZ where it reaches values around 320 HVIT. Although no significant modification of the microstructure in terms of phases present and grain size, the reduction of hardness in the stirred zone is consistent with the lower density of local misorientation maps of the welds when compared with the original conditions of the BM, as depicted in Fig. 9k–o. There is a slightly higher hardness zone (270 HVIT) inside the stirred zone of the Slow and the Fast welds (i.e., those

without active cooling) at the AS near the root. This effect is likely due to a local concentration of precipitates led by the material flow during the FSW process, which can be observed in the macrographs of Fig. 5a, b. In the welds without active cooling, the HAZ at the RS exhibits a somewhat higher hardness than the HAZ at the AS. The hardness distribution at the HAZ around the stirred zone is mostly symmetric for the welds with active cooling. The highest value measured was 407 HVIT in the HAZ at the RS for the slow weld condition. Details of the microstructure around the indentations in this zone, and in BM, are presented in Fig. 11. According to the values presented in Table 3, this zone of the Slow weld condition, at 7.5 mm from the joint line into the RS, underwent a period over the critical temperatures A_1 and A_3 of about 14 and 6 s, respectively. Although the size and shape of prior austenite were not possible to assess with the experimental method implemented, the original fine ferritic-bainitic microstructure was recrystallized locally into a harder microstructure with coarser grains, as quantified in Fig. 8. This effect is not present in any of the remaining weld conditions.
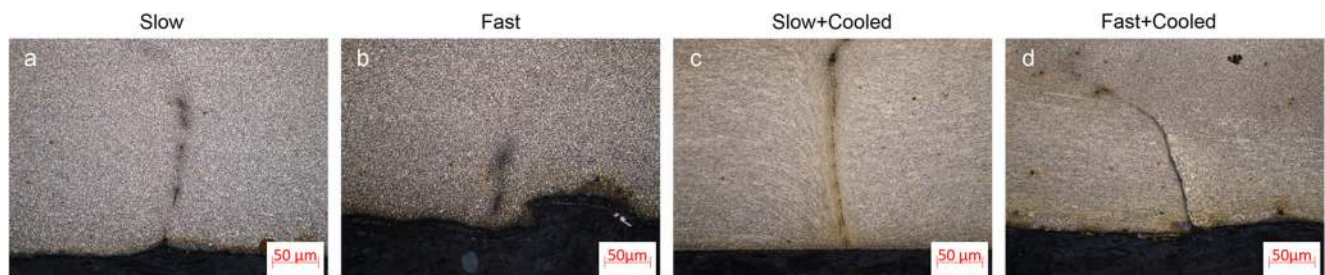

Fig. 6 Micrographs of the welded samples showing in detail the weld root at × 20 magnification to emphasize the different types, extensions, and paths of the defects at this zone of the tested weld conditions. **a** Slow weld with alignment of particles. **b** Fast weld with alignment of particles, but smaller than in Slow weld. **c** Slow + Cooled weld with long LOP progressing sharply into the stirred zone as alignment of particles. **d** Fast + Cooled weld short LOP progressing into deflected alignment of particles
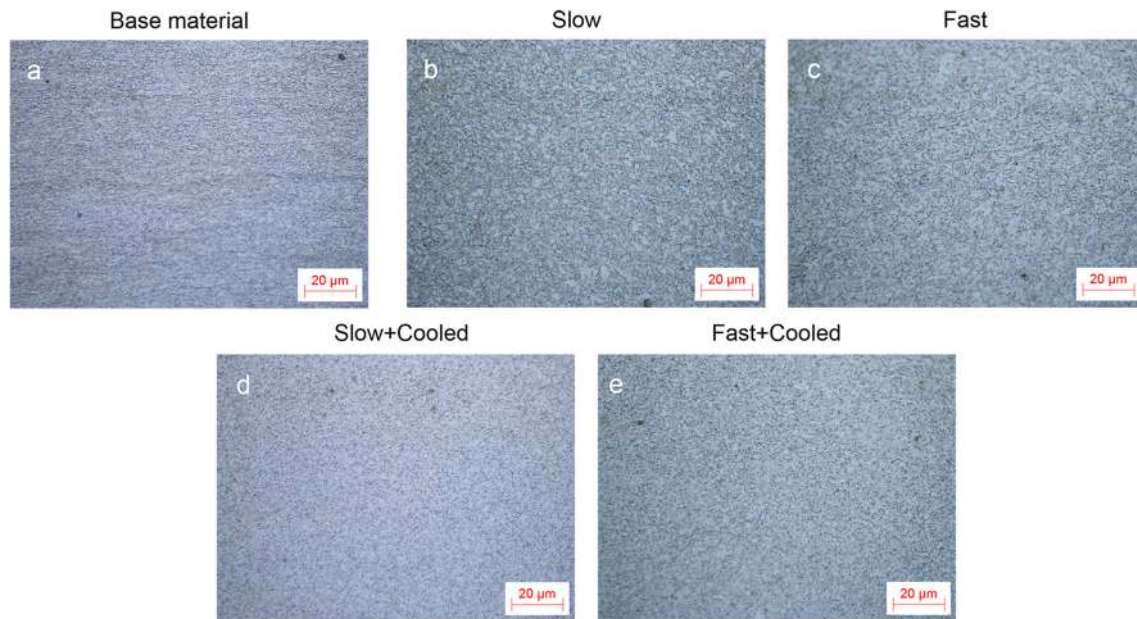
Fig. 7 Micrographs (× 50 magnification) of the base material and middle of the stirred zone (as marked with a yellow square in Fig. 5) of the four different weld conditions. **a** Base material. **b** Slow weld. **c** Fast weld. **d** Slow + Cooled weld. **e** Fast + Cooled weld

3.4 Bending and tensile test results

To decouple the effects of the incomplete penetration from the microstructural changes induced by the thermomechanical processing during the FSW cycle, half of the specimens for tensile test were milled on the root side (0.5 mm), effectively removing any possible LOP defects. The same procedure was carried out for one specimen for bending test, per condition, with the root on the tensile side. The mechanical test results will show data for machined and non-machined conditions.

The results of the bending tests (Fig. 12) with the face side in tensile displayed an efficiency between 90 and 94% for all the weld conditions. The root defect plays an important role in all the tests with the root in tensile (efficiency less than 60%), with the exception of the Slow weld condition which exhibited a high efficiency (96%). The machined specimens tested with the root side under tensile load have an efficiency between 79 and 84%, slightly lower than with the face side under tensile load. In general, the weld conditions only affected the resistance under bending load if the root defect reaches a relevant size, e.g., over 50 μm of continuous alignment of particles or LOP. To support the analysis of the results from the bending tests, Fig. 12b includes a line marking the limit force calculated to reach the plastic moment, $F_{Eurocode3}$ (1), according to the weld design standard EN 1993-1-8:2005 [33]. This standard on the design of joints in steel structures does not encompass HSS with the grade of the tested material, but is the closest guideline on this issue. In almost all the samples, the bending strength is above the limit value $F_{Eurocode3}$ (1). The only exceptions are the as-welded samples from the + Cooled weld conditions, with the root side under tensile load, where the LOP was more relevant (Fig. 6). This suggests that, under bending loading, this friction stir-welded HSS is more sensitive to the technological conditions controlling the tool penetration than to the metallurgical properties resulting from the weld cycle.

Fig. 8 Grain size distribution along the cross-section of the weld of each of the four different FSW conditions
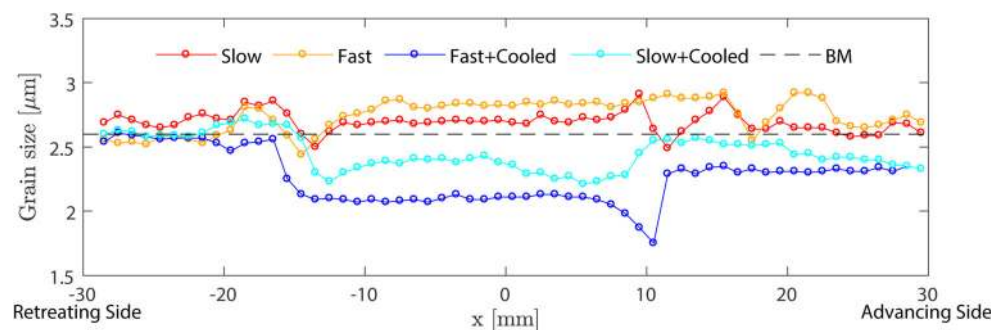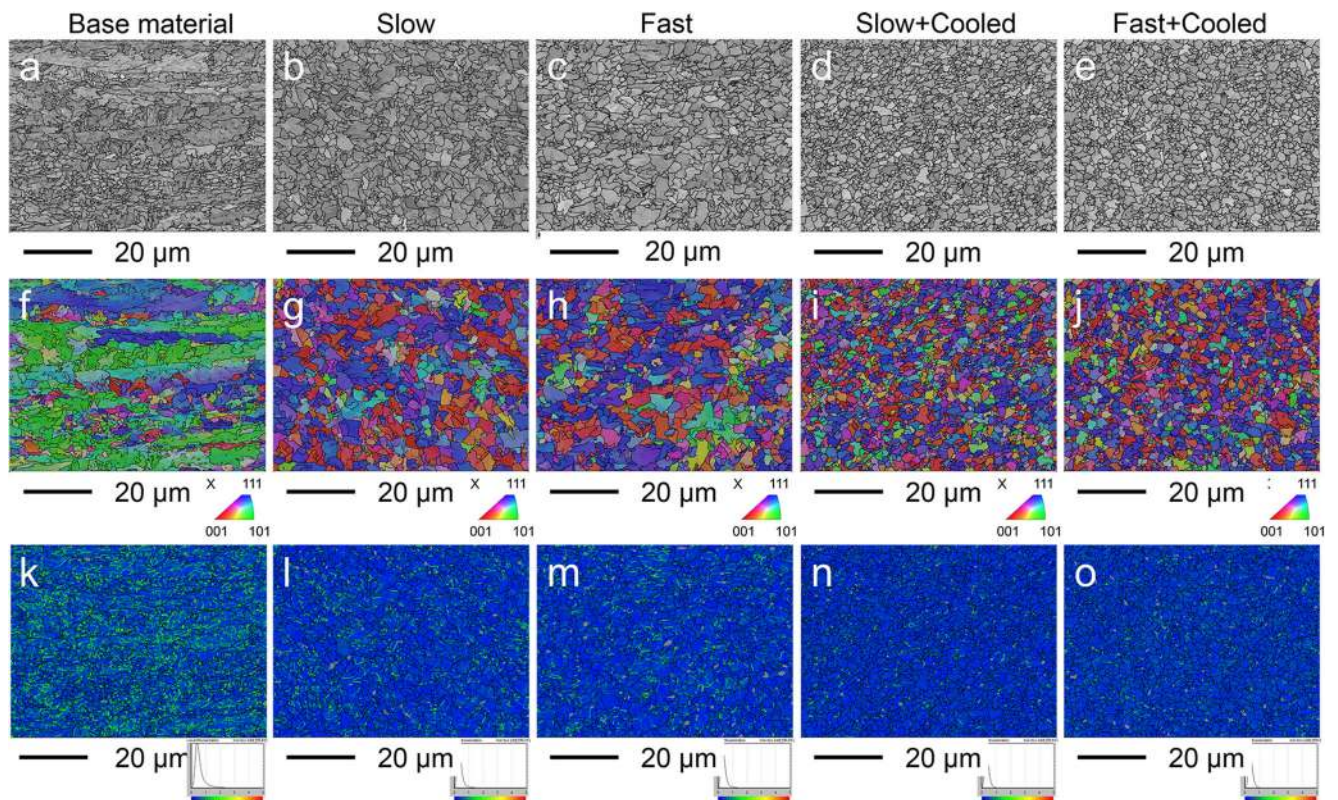
Fig. 9 EBSD images for the base material and for the stirred zones of the different weld conditions. **a–e** Band contrast images. **f–j** Inverse pole figures showing the orientation of the microstructure. **k–o** Local misorientation maps

$$\frac{M_{Ed}}{M_{c,Rd}} \leq 1.0 \Longleftrightarrow \frac{F_{Eurocode3}.d}{4} \leq \frac{f_y}{\gamma_{M0}} \frac{t^2.w}{4} \Rightarrow (F_{Eurocode3})_{max}$$
$$= 3.3 \; kN \tag{1}$$

where M_{Ed} is the design bending moment; $M_{c, Rd}$ is the plastic bending moment about the principal axis of the sample cross-section; f_y is the nominal yield strength (f_y=700 MPa); γ_{M0} is the partial material safety factor (γ_{M0}=1.0); t is the thickness of the sample (t = 4 mm); w is the width of the sample (w = 16 mm); d is the distance between the roller supports in the

three-point bending test (d = 54 mm).

Figure 13 displays the tensile test results, which reveal a strength decrease in all weld conditions, in relation to the BM level. There is a reduction in yield strength from the original 787 to 537–571 MPa, which means a strength efficiency of about 70%. The reduction in ultimate tensile strength (UTS) is about 21%. The strain localization always occurs at the middle of the weld, within the stirred zone, as shown by the DIC images in Fig. 14. This localization effect is less pronounced when there is no relevant root defect, such as in the Slow weld condition. In fact, only the Slow weld condition exhibits the
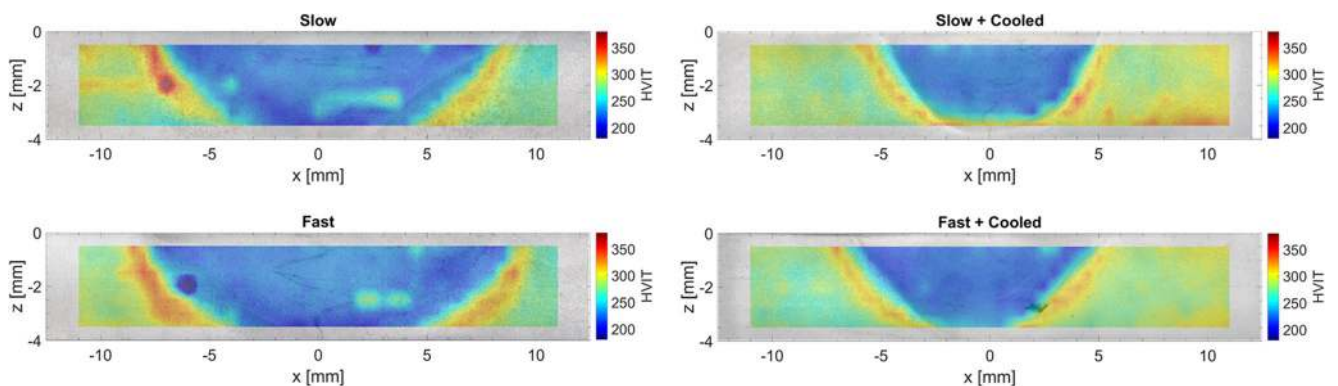

Fig. 10 Hardness (HVIT) distribution maps superimposed on macrograph of the four different weld conditions
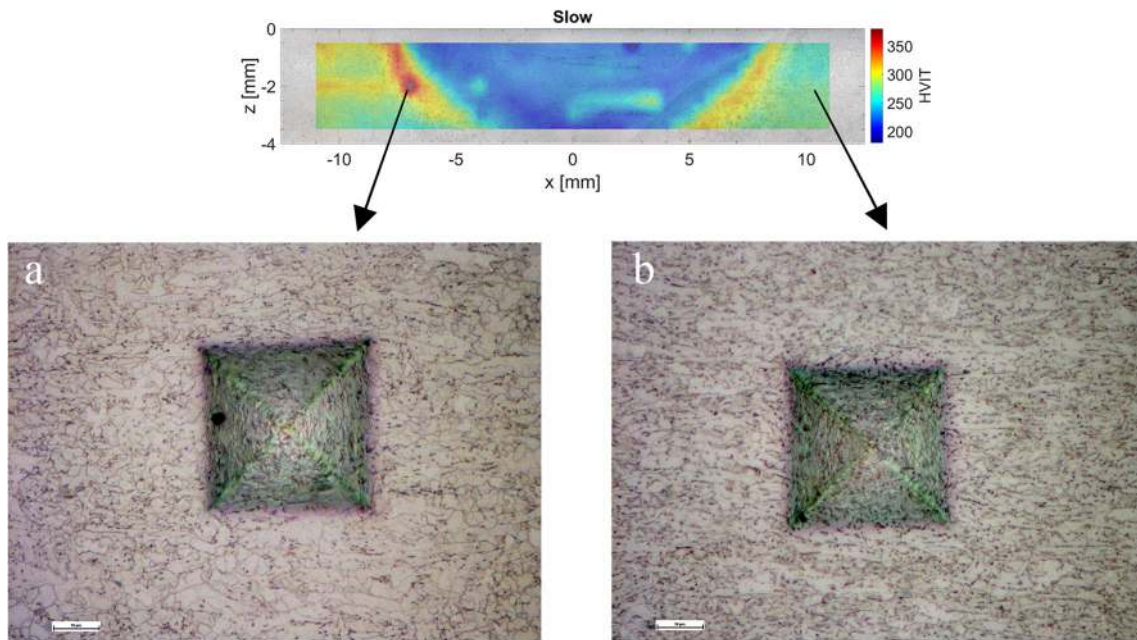
Fig. 11 Local microstructures in the vicinity of hardness indentations at important zones. (a) Indentation where the highest hardness value was reached, at the RS in HAZ of Slow welding condition. (b) Indentation in the BM

same deformation pattern in the as-welded as in the machined specimens at both the UTS and before fracture. In general, the different weld conditions and the small root defect did not lead to different weld strength under tensile loading. In accordance with the weld design standard for steel structures EN 1993-1-8:2005 [33], the design resistance of a full penetration butt weld should provide tensile specimens having both a minimum yield strength and a minimum UTS not less than those specified for the BM. If future design standards encompassing this grade of HSS will enable undermatching tensile strength of the weld zone in relation to the tensile strength specified for the BM, then FSW can be included as one technological solution for these welds.

3.5 Charpy impact test results

The effect of the welded zone on the impact toughness is a major challenge to the weldability of HSS [29]. Figure 15 shows the Charpy impact test results for the FSW of this S700MC steel at − 40 and − 60 °C, measured at the three locations indicated in Fig. 3. All the weld zones of all the weld conditions closely match, and in most of the situations even overmatch, the base material properties (41 J@-40 °C; and 39 J@-60 °C). The behavior in all the weld conditions repeats at both temperatures. Namely, the stirred zone is the best zone of the weld in the Fast + Cooled and the worst in the
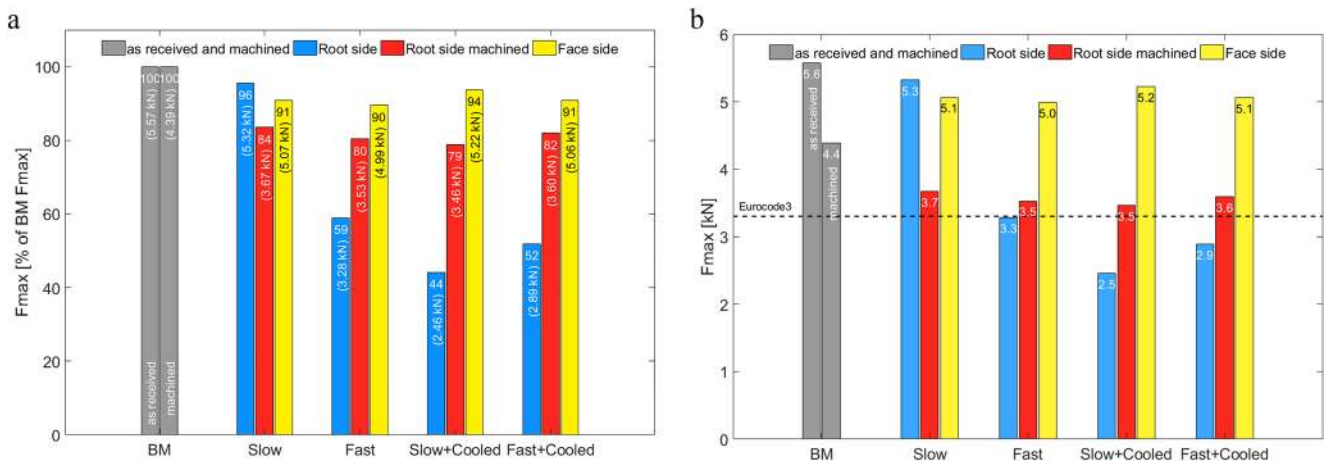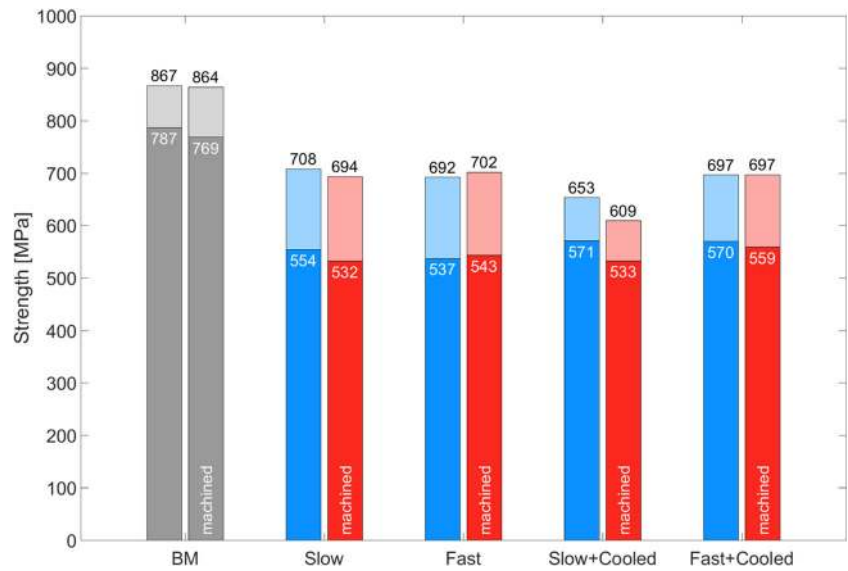

Fig. 12 Maximum bending force with results for all the four weld conditions. **a** Results presented in percentage relative to the BM. **b** Absolute values, including the $(F_{Eurocode3})_{max}$

Fig. 13 Tensile test results showing the ultimate tensile strength (UTS) and yield strength of the base material (BM) and the four different weld conditions

Slow welds. The Fast weld condition exhibits the best overall impact toughness results, overmatching the toughness of the base material at both temperatures in all the weld regions (37 to 69% higher than the base material). The Slow + Cooled weld performs the worst at both temperatures. This result is not supported by the microstructure analysis, mainly when compared with the Fast + Cooled weld conditions, at the center of the stirred zones, that are very similar (Fig. 9d, i, n for the Slow + Cooled weld condition and Fig. 9e, j, o for the Slow + Cooled weld condition and Fig. 9e, j, o for the Slow + Cooled weld condition and Fig. 9e, j, o for

for the Fast + Cooled weld condition). However, this effect may be induced by the slightly larger LOP presented in Fig. 6 and described in Section 3.2. In this weld condition, the LOP and alignment of particles progress deep into the stirred zone, reducing its effective thickness. The RS is distinguishably better than the AS for the Slow and Fast welds (i.e., those without active cooling) but the difference is negligible for the welds with active cooling, which is in agreement with the hardness maps presented in Fig. 10.
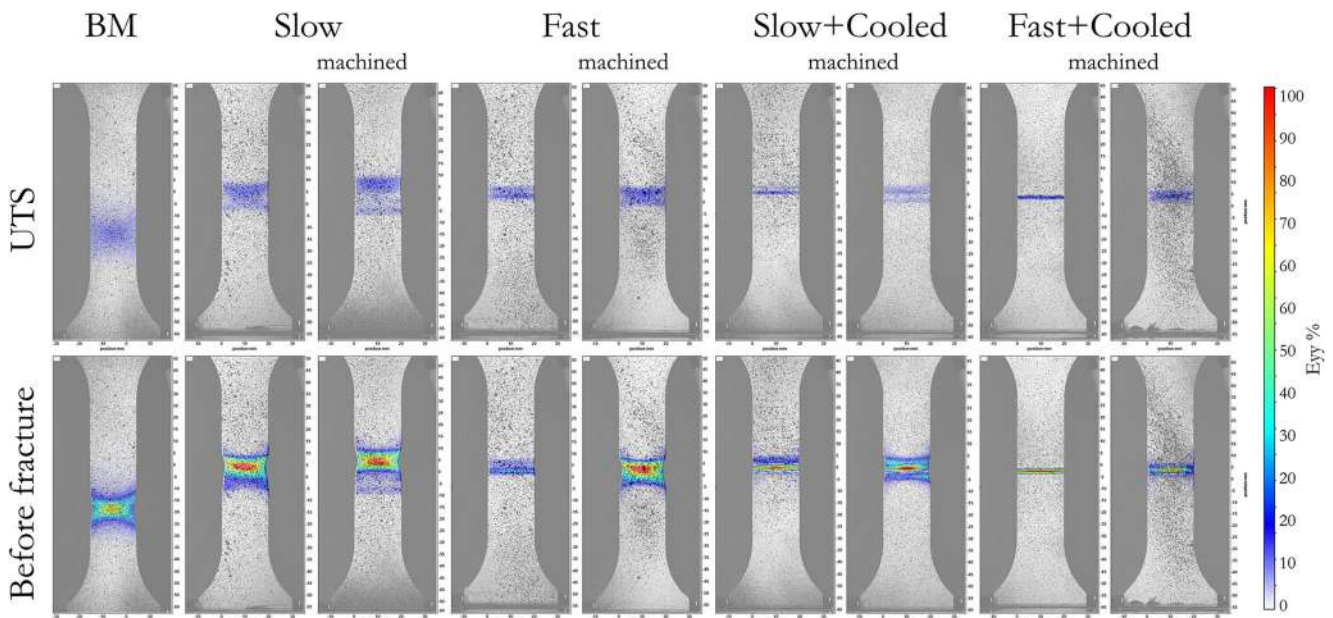

Fig. 14 Digital image correlation (DIC) images monitoring the strain field during the tensile tests, for the base material (BM) and the four different weld conditions, with specimens in as-welded and machined condition. The strain field is presented at the moment when the UTS is reached (top) and immediately before fracture (bottom)
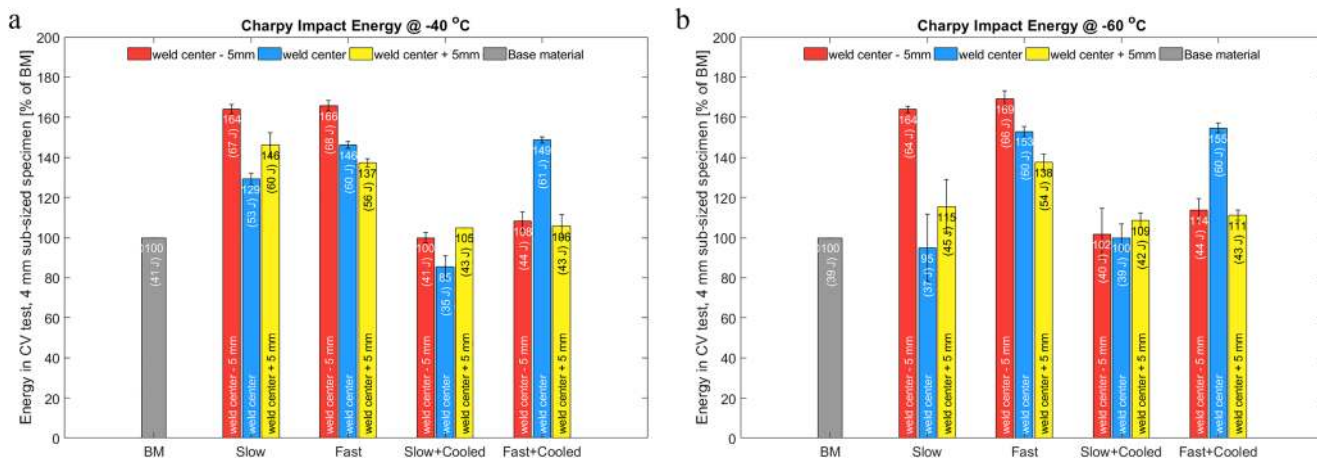
Fig. 15 Charpy impact results at the weld center − 5 mm (i.e., retreating side), weld center (i.e., center of stirred zone), and weld center + 5 mm (i.e., advancing side). The results are presented in absolute values and in percentage relative to the base material (BM). **a** Test at − 40 °C. **b** Test at − 60 °C

4 Conclusions

The different weld conditions tested demonstrate the feasibility of FSW of HSS within the intercritical temperature domain with important benefits to the final properties. The range of peak temperatures measured at 5 mm from the joint line was between 906 °C (Slow weld condition) and 656 °C (Fast + Cooled weld condition). Emphasis should be given to the fact that, without a severe compromise of the original high-strength performance, a very significant improvement of the toughness was obtained. Namely, the Fast weld condition, with a measured peak temperature of 761 °C, exhibited an impact toughness, in all the weld sub-regions, significantly overmatching the toughness of the base material. In more detail, the main conclusions are as follows:

- The active cooling of the clamping system plays a more relevant role than the weld pitch ratio (Ω/v) in controlling the peak temperature and the heating and cooling rates. The cooling in the Slow + Cooled and Fast + Cooled conditions was twice as fast as in the Slow and Fast conditions, respectively. Consequently, the width of the processed zone and HAZ is narrower in the active cooled welds. Also, the hardness distribution at the HAZ, around the stirred zone, is more symmetric for the welds with active cooling.

- FSW of S700MC+ produced a stirred zone with fine equiaxed grains, retaining some of the original ferritic-bainitic microstructure but altering grain orientation. The original grain size of about 2.6 μm was marginally increased for the welds without active cooling, and a trend of reduction of this value with active cooling is evident. The local misorientation maps from the EBSD analysis show higher strain concentration in the base material than in the stirred zone of the welds. This justifies the higher hardness values in the BM compared to the stirred zone of all the weld conditions despite the similar grain sizes.

- The extremely cold FSW conditions of the Fast + Cooled weld led to defects in the stirred zone, such as voids and root defects. The bending efficiency of the FSW welds was over 79%, compared to the BM, and the results show no sensitivity to the weld conditions except if the root defect reaches a relevant size. The FSW yield strength efficiency was about 70% of the BM. The reduction in ultimate tensile strength (UTS) was about 21%. In general, neither the weld condition nor the small root defect affected the strength of the weld under tensile loading condition.

- In all the weld sub-zones, and for all the weld conditions tested, the impact toughness of the FSW welds matched or overmatched the base material properties. The Fast weld condition exhibited the best overall impact toughness results, overmatching the toughness of the BM in over 137% at both − 40 and − 60 °C.

References

1. Bhadeshia H, Honeycombe R (2017) Steels: microstructure and properties. Butterworth-Heinemann
2. Vilaça P, Quintino L, Dos Santos JF (2005) ISTIR—analytical thermal model for friction stir welding. J Mater Process Technol 169: 452–465. https://doi.org/10.1016/j.jmatprotec.2004.12.016
3. Philip T V., McCaffrey TJ (1990) Ultrahigh-strength steels. In: Prop. Sel. Irons, steels, high-performance alloy. pp 430–448
4. Keeler S, Kimchi M (2014) Advanced high-strength steels application guidelines version 5.0. World AutoSteel.org 511. doi:https://doi.org/10.1016/S1644-9665(12)60197-6

5. Hall AM (1971) Introduction to today's ultrahigh-strength structural steels. ASTM International

6. Tamura I, Sekine H, Tanaka T (2013) Thermomechanical processing of high-strength low-alloy steels. Butterworth-Heinemann

7. Dhua SK, Sen SK (2011) Effect of direct quenching on the microstructure and mechanical properties of the lean-chemistry HSLA-100 steel plates. Mater Sci Eng A 528:6356–6365. https://doi.org/10.1016/j.msea.2011.04.084

8. Fukumoto Y (1996) New constructional steels and structural stability. Eng Struct 18:786–791. https://doi.org/10.1016/0141-0296(96)00008-9

9. Vilaça P, Thomas W (2012) Friction stir welding technology. In: Moreira PMGP, da Silva LFM, de Castro PMST (eds) Struct. Connect. Light. Met. Struct. Springer, Berlin, pp 85–124

10. Vidal C, Infante V, Vilaça P (2009) Fatigue behaviour in friction stir welded joints of AA2024 treated by improvement techniques. Weld World 53:241–246

11. Taavitsainen T, Vilaça P, Mutanen T (2016) Production by FSW of free-shape hollow box profile in AA5754 for automotive application. Weld World 60:1121–1131. https://doi.org/10.1007/s40194-016-0382-0

12. Leal RM, Leitão C, Loureiro A, Rodrigues DM, Vilaça P (2010) Microstructure and hardness of friction stir welds in pure copper. Mater Sci Forum 636-637:637–642. https://doi.org/10.4028/www.scientific.net/MSF.636-637.637

13. Savolainen K, Saukkonen T, Mononen J, Hänninen H (2008) Entrapped oxide particles in friction stir welds of copper. 7th Int. Symp. Frict. Stir Weld

14. Bobby Kannan M, Dietzel W, Zeng R, Zettler R, dos Santos JF (2007) A study on the SCC susceptibility of friction stir welded AZ31 Mg sheet. Mater Sci Eng A 460–461:243–250. https://doi.org/10.1016/j.msea.2007.01.065

15. McPherson NA, Galloway AM, Cater SR, Hambling SJ (2013) Friction stir welding of thin DH36 steel plate. Sci Technol Weld Join 18:441–450. https://doi.org/10.1179/1362171813Y.0000000122

16. Gomes JFP, Albuquerque PCS, Miranda RMM, Vieira MTF (2012) Determination of airborne nanoparticles from welding operations. J Toxicol Environ Health A 75:747–755. https://doi.org/10.1080/15287394.2012.688489

17. Thomas WM, Threadgill PL, Nicholas ED (1999) Feasibility of friction stir welding steel. Sci Technol Weld Join 4:365–372. https://doi.org/10.1179/136217199101538012

18. Rai R, De A, Bhadeshia HKDH, DebRoy T (2011) Review: friction stir welding tools. Sci Technol Weld Join 16:325–342. https://doi.org/10.1179/1362171811Y.0000000023

19. Perrett J, Martin J, Peterson J, et al (2011) Friction stir welding of industrial steels. In: Frict. Stir Weld. Process. pp 1–5

20. Azevedo J, Infante V, Quintino L, dos Santos J (2014) Fatigue behaviour of friction stir welded steel joints. Adv Mater Res 891–892:1488–1493. doi: https://doi.org/10.4028/www.scientific.net/AMR.891-892.1488

21. Lienert T, Jr WS (2003) Friction stir welding studies on mild steel. Weld J Res Suppl 82:1–9

22. Reynolds AP, Tang W, Posada M, Deloach J (2003) Friction stir welding of DH36 steel. Sci Technol Weld Join 8:455–460. https://doi.org/10.1179/136217103225009125

23. Fujii H (2008) Friction stir welding of steels. J Japan Weld Soc 77:731–744. https://doi.org/10.2207/jjws.77.731

24. Wei L, Nelson TW (2012) Influence of heat input on post weld microstructure and mechanical properties of friction stir welded HSLA-65 steel. Mater Sci Eng A 556:51–59. https://doi.org/10.1016/j.msea.2012.06.057

25. Cui L, Fujii H, Tsuji N, Nakata K, Nogi K, Ikeda R, Matsushita M (2007) Transformation in stir zone of friction stir welded carbon steels with different carbon contents. ISIJ Int 47:299–306. https://doi.org/10.2355/isijinternational.47.299

26. Fujii H, Cui L, Tsuji N, Maeda M, Nakata K, Nogi K (2006) Friction stir welding of carbon steels. Mater Sci Eng A 429:50–57. https://doi.org/10.1016/j.msea.2006.04.118

27. Cui L, Fujii H, Tsuji N, Nogi K (2007) Friction stir welding of a high carbon steel. Scr Mater 56:637–640. https://doi.org/10.1016/j.scriptamat.2006.12.004

28. El-Batahgy AM, Miura T, Ueji R, Fujii H (2016) Investigation into feasibility of FSW process for welding 1600MPa quenched and tempered steel. Mater Sci Eng A 651:904–913. https://doi.org/10.1016/j.msea.2015.11.054

29. Peltonen M Weldability of high-strength steels using conventional welding methods; Suurlujuusterästen liittäminen perinteisillä hitsausmenetelmillä. Aalto U

30. Lahtinen T (2016) Analysis and development of weldability of novel 700 mpa high strength steels. Tampere University of Technology

31. Olson DL, Siewert TA, Liu S, Edwards GR (1993) ASM handbook volume 6 - welding brazing and soldering

32. Krauss G (2015) Steels: processing, structure, and performance. ASM Int 30:627–628. https://doi.org/10.1037/023990

33. European Standards Organisation (2005) Eurocode 3: design of steel structures—part 1–8: design of joints